Formation of Cellulose Acetate - Graphene Oxide Nanocomposites by Supercritical CO_2 Assisted Phase Inversion

Lucia Baldino,[a] *Maria Sarno,*[a,b,*] *Stefano Cardea,*[a,*] *Silvia Irusta,*[c] *Paolo Ciambelli,*[a,b] *Jesus Santamaria*[c] *and Ernesto Reverchon*[a,b]

a Department of Industrial Engineering, University of Salerno, Via Giovanni Paolo II, 132, 84084, Fisciano (SA), Italy.
b NANO_MATES, Research Centre for Nanomaterials and Nanotechnology, University of Salerno, Via Giovanni Paolo II, 132, 84084, Fisciano (SA), Italy.
c Nanoscience Institute of Aragon (INA) and Networking Biomedical Research Center of Bioengineering, Biomaterials and Nanomedicine (CIBER-BBN), 50018, Zaragoza, Spain.

* Corresponding Authors. Email: scardea@unisa.it (Stefano Cardea) Phone Number: +39089969365; msarno@unisa.it (Maria Sarno) Phone Number: +39089964057.

KEYWORDS**:** Graphene oxide, Cellulose acetate, Nanocomposite, Supercritical CO_2.

ABSTRACT

Cellulose acetate (CA)/graphene oxide (GO) nanocomposite membranes were generated by an assisted phase inversion process, based on the use of SC-CO_2 as non-solvent, operating at 200 bar and 40 °C; loadings of GO up to 9% w/w were tested. The structures maintained the cellular morphology, characteristics of CA membranes, also at the highest GO loadings used, with a porosity of about 80%, but the presence of GO influenced the pore sizes, that ranged between about 9 and 16 µm. The starting GO and the nanocomposite structures were characterized by the combination of various techniques that evidences as Sulphur and Chlorinated impurities, that were present in the starting GO material, were completely eliminated by the interaction with SC-CO_2 during structures formation; moreover, a partial reduction of GO to graphene was also observed.

1. INTRODUCTION

Graphene oxide (GO) is commonly synthesized by oxidation of graphite using strong mineral acids and oxidizing agents, typically via treatment with $KMnO_4$ and H_2SO_4 using the Hummers method[1]. Compared to graphene, GO is heavily oxygenated and its basal plane carbon atoms are decorated with epoxide and hydroxyl groups and its edge atoms with carbonyl and carboxyl groups. Hence, GO is highly hydrophilic and the presence of these functional groups reduces interplanar forces, which can improve the interfacial interaction between GO and some polymers and, thus, the dispersion of GO in polymer matrices[2, 3]. Many factors can affect the final properties and applications of GO/polymer nanocomposites[4], among these: kind of GO used, its dispersion state in the polymeric matrix and interfacial interactions, the amount of wrinkling, its network structure in the matrix and its purity.

Various attempts have been proposed in the literature to realize GO/polymers composite structures[5-15]. The processes proposed until now (*i.e.*, phase inversion, casting, electrospinning) present several limitations; for example, residues of organic solvents of GO synthesis are typically found at the end of these processes, causing problems, in particular, for biomedical applications. Moreover, a homogeneous distribution of GO in the polymeric matrix is difficult to obtain, since the cohesive forces among GO layers tend to produce restacking. GO composites performance is strongly related to its level of exfoliation (*i.e.*, separation of the layers). Exfoliated GO allows the largest interfacial contact with the polymer matrix, improving the properties of the composites. For this reason, several techniques have been implemented to increase the GO exfoliation degree. In particular, solvent-based exfoliation and thermal exfoliation techniques emerged as two preferred routes for this step[16-19]. These techniques achieved encouraging results, but, still present many limitations; for example: high cost, use of

large quantities of hazardous chemicals, high heating temperatures that can induce degradation of the polymeric matrix.

A possible way to overcome the above mentioned limitations, is the use of supercritical carbon dioxide (SC-CO_2) assisted processes. Indeed, supercritical fluids (SCFs) possess near-zero interfacial tension and a density that can be tuned from gas- to liquid-like values. These characteristics, along with the excellent wetting of surfaces and high diffusion coefficients, made SCFs useful to overcome the limitations of several traditional techniques; for example, to control microparticles size[20-22] and to extract natural matters[23]. SCFs techniques have been used to produce polymeric structures with controlled morphology and porosity[24-26]. Membranes and aerogels loaded with pharmaceutical compounds[27], catalyst[28] and active agents for packaging applications[29] have also been proposed using these techniques. Homogenous composite structures with controlled morphology and very reduced residual solvents were obtained, confirming the possibility of overcoming the limits of the traditional procedures. SCFs assisted techniques have been already used in graphene processing. In particular, a supercritical exfoliation method has been tested[30-33]. Due to molecular size of CO_2 and its polarizability, it has the potential to pass through the solid porous layers[34] and, when supercritical conditions are reached, CO_2 diffusivity can favor layers expansion and exfoliation[31-33]. It is also possible to add co-solvents (*e.g.*, N-methylpyrrolidone (NMP), DMF and Isopropanol), to increase the polarity and the fluid-solid interaction[30].

Therefore, the aim of this work is to obtain homogenous Cellulose Acetate (CA)-GO nanocomposite membranes controlling the interactions of GO layers and their behavior in a polymeric matrix, using SC-CO_2 assisted phase inversion[25]. The scope is to combine the advantages of SC-CO_2 assisted loading techniques with the possibility of controlling the incorporation of GO. CA has been selected as the polymeric matrix, due to its numerous

potential applications; for example, as scaffold in cartilage regeneration[35], neural differentiation[36] cardiac applications[37], in dialysis membranes[38] and in ultrafiltration devices[39]. We verified the process feasibility and its implications on GO composition and layers arrangement. We also analyzed the effect of different GO loadings on morphology, pore size and on mechanical and physico-chemical characteristics of the nanocomposite membranes.

2. MATERIALS AND METHODS

2.1 Materials

CA (average Mn *ca.* 50 000 with acetyl content of 39.7%) and NMP (purity 99.7%) were bought from Sigma-Aldrich. CO_2 (99.5% purity) was purchased form SON (Società Ossigeno Napoli, Italy). All materials were used as received.

2.2 Graphene oxide synthesis

GO was prepared according to the modified Hummers method[40]. In a typical procedure, graphite (1.0 g) was mixed with 23 mL of H_2SO_4 (95%) and the mixture was stirred for 30 min within an ice bath. Potassium permanganate (3.0 g) was added very slowly to the suspension, with vigorous stirring, while maintaining a reaction temperature of 20 °C. The ice bath was removed and the reaction mixture was stirred overnight at 35 °C. Then, water was added to the pasty solution with constant agitation: the colour of the solution changed to yellowish brown. After 2 h of vigorous stirring, 25 mL of 30% H_2O_2 were added and immediately the colour of the solution turned to golden yellow. The mixture was washed several times with 5% HCl and, then, with deionized water, until the solution became acid free. At the end of the process, the reaction mixture was filtered and dried under vacuum at 65 °C.

2.3 Preparation of CA/GO nanocomposite membranes

We produced CA/GO nanocomposites by a SC-CO_2 assisted phase inversion process[25]. First, solutions of CA in NMP with a concentration of 25% w/w were prepared. Subsequently, GO was suspended in the polymeric solution at different concentrations: 3 and 9% w/w with respect to the polymer content. GO concentrations were selected studying the scientific literature that reports as these amounts of GO are enough to modify/improve the properties of a polymeric matrix (i.e., nanocomposite). The ternary system (CA/NMP/GO) was stirred at room temperature until it became a stable suspension. Then, the suspension was spread on steel caps (of about 2 cm diameter and 200 µm height) inside a custom-made high pressure vessel and phase separated using SC-CO_2 at 200 bar and 40 °C for 4 h (or 8 h), with a CO_2 flow rate of about 2 Kg/h. In particular, the vessel was filled with SC-CO_2, up to the desired pressure, using a high pressure pump (Milton Roy-Milroyal B, Pont-Saint-Pierre, France). The pressure was controlled by a manometer (mod. MP1, OMET, Italy) and the temperature was set by a controller (mod. 305, Watlow, Italy). A depressurization time of 30 min was used to bring back the system at atmospheric pressure.

In the remainder of this work, the samples generated will be noted as CA_GO_1 and CA_GO_2, for GO fillings of 3 and 9% w/w, respectively. A longer experiment has been also performed on GO 9% w/w polymeric solution (at 200 bar and 40 °C, for 8 h) and the sample generated with this procedure will be noted as CA_GO_2_8h.

2.4 Field Emission Scanning Electron Microscopy (FESEM)

CA/GO nanocomposites were cryofractured using liquid Nitrogen; then, the sample was sputter coated with Gold (Agar Auto Sputter Coater mod. 108 A, Stansted, UK) at 30 mA for

150 s and was analyzed by FESEM (mod. LEO 1525, Carl Zeiss SMT AG, Oberkochen, Germany) to analyze pore size and the overall structure morphology.

Sigma Scan Pro 5.0 (Jandel Scientific, San Rafael, CANADA) and Origin 8.5 (Microcal, Northampton, USA) softwares were used to determine the average diameter of pores in the structure. Images taken at various locations in the structure were used for each calculation. We measured about 300 pores for each sample analyzed. Using Origin software, we first represented a histogram with the percentage of the pores having a given diameter; then, we performed a curve fitting by lognormal function to obtain the distribution curves.

2.5 Nanocomposite porosity

Porosity (ε) represents the "void space" of the structure; it was calculated using the ratio of the apparent volume to the true volume of the structures. An ultrapycnometer (Ultrapycnometer 1000, Quantachrome instruments, Florida, USA) was used to measure the true volume of the structures at 25 °C in pure Argon; three measurements were made on each specimen and the mean was used in the porosity calculations. The apparent volume of the structures was calculated from measurement of their external dimension, using a digital calliper.

2.6 Differential Scanning Calorimetry (DSC)

DSC analysis (DSC 30 Mettler, Toledo) was carried out to analyze and identify any change in the thermograms of pure substances compared to CA/GO formulations. Calorimetric analysis was performed in the temperature range between 0 and 300 °C, with a heating rate of 10 °C/min; the inert gas was Nitrogen.

2.7 Thermogravimetric Analysis (TGA)

The thermal decomposition behavior was investigated using a thermo-analyzer (Q600, TA Instruments) online connected to a quadrupole mass detector (Quadstar 422, Pfeiffer Vacuum, USA). The measurement was carried out in 1% v/v O_2 in N_2 and in air flow.

2.8 X-Ray Diffraction (XRD)

XRD measurements were performed using a Bruker D8 X-ray diffractometer (USA) with CuKα radiation. The measurements were performed on the powder obtained after filtration. GO X-ray diffraction measurements were taken using a D-Max Rigaku equipped with a rotating anode. The diffractometer operated at 40 kV and 80 mA using with Cu anode and graphite monochromator used to select the radiation CuKα1,2, using a scanning rate of 0.03º.seg -1. The range of measurement varied between 5 and 50º. The filtration results in a thin carbon film, that after drying consists of a fine and light powder, which was loaded in the XRD sample holder to full a window of 2 cm in diameter. Before the measurements, the sample was leveled to the holder surface using a glass slide.

2.9 Transmission Electron Microscopy (TEM)

TEM images were acquired using a FEI Tecnai electron microscope, operating at 200 kV with a LaB_6 filament as the source of electrons, equipped with an Energy Dispersive X-ray Spectroscopy (EDX) probe. The specimens for TEM analysis were prepared by suspending GO in water, homogeneizing the suspension and allowing a drop of this suspension to evaporate on an amorphous carbon-coated Cu grid.

2.10 Raman spectroscopy

Raman spectra were obtained at room temperature with a microRaman spectrometer (Renishaw inVia, UK, 514 nm excitation wavelength, laser power 30 mW). A Leica DMLM optical microscope is connected on-line with the Raman instrument to focus on the sample. The laser spot diameter was 10 μm, a value higher than the size of the GO sheets. The measurements were performed on the powder obtained after filtration. The filtration results in a thin carbon film, that after drying consists of a fine and light powder, that was loaded for the measurements on glass slide.

2.11 X-Ray photoelectron spectroscopy (XPS)

XPS analyses were performed with an Axis Ultra DLD (Kratos Tech.). The spectra were excited by the monochromatized AlKα source (1486.6 eV) run at 15 kV and 10 mA. GO powder was pressed onto a Copper tape mounted on a sample rod that was, then, introduced into the pretreatment chamber of the spectrometer and evacuated at room temperature. For the individual peak regions, a pass energy of 20 eV was used. Analyses of the peaks were performed with the CasaXPS software, using a weighted sum of Lorentzian and Gaussian components curves after background subtraction.

3. RESULTS AND DISCUSSION

3.1 GO characterization

TEM images of GO produced in this work are shown in Figure 1: thin layers with sizes in the range of half to tens of square microns were observed. GO exhibits a rough surface showing wrinkles[41,42]. It has been reported that during the drying process of GO, water exerts surface tension due to high affinity to GO oxidized domains[43], inducing stresses during evaporation[44], which force the soft sheets to fold and wrinkle[45, 46] and/or can exacerbate the wrinkled

structure[43]. In particular, in Figures 1E and 1F nanosheets edges of about 5 nm can be detected that correspond to the largest thickness observed in the sample. In the regions indicated by the arrows in Figures 1E and 1F, 6 and 4 twisted layers can be seen, respectively. These observations indicate that the starting GO material was organized as few-layers graphene; *i.e.*, it was partly exfoliated. Thinner nanosheets can be seen in Figure 1G. Figure 1C shows the energy dispersive TEM based EDX of the prepared sample, with a carbon/oxygen (C/O) ratio of ~2.6 at, that is a value comparable to those typically reported in the literature[56]. Small amounts of S and Cl, confirmed by the TG-MS analysis (Figure 1S and 2S), deriving from GO preparation process are also present; indeed, it is known that even a very accurate washing process cannot completely remove these species from GO[47].

The formation of oxygenated groups due to the oxidation of graphite is confirmed by XRD (Figure 3SA), Raman Spectroscopy (Figure 3SB) and XPS. In particular, the C/O ratio, calculated from C 1s and O 1s core level spectra, decreased from 58.9 to 2.5 after the oxidation process, clearly indicating a considerable degree of oxidation. The C 1s XPS spectrum of GO, shown in Figure 2, exhibited the characteristic peaks of C–C skeleton, hydroxyl, epoxyl and carbonyl groups at 284.4, 286.4, 287.7 and 288.7 eV, respectively[48].

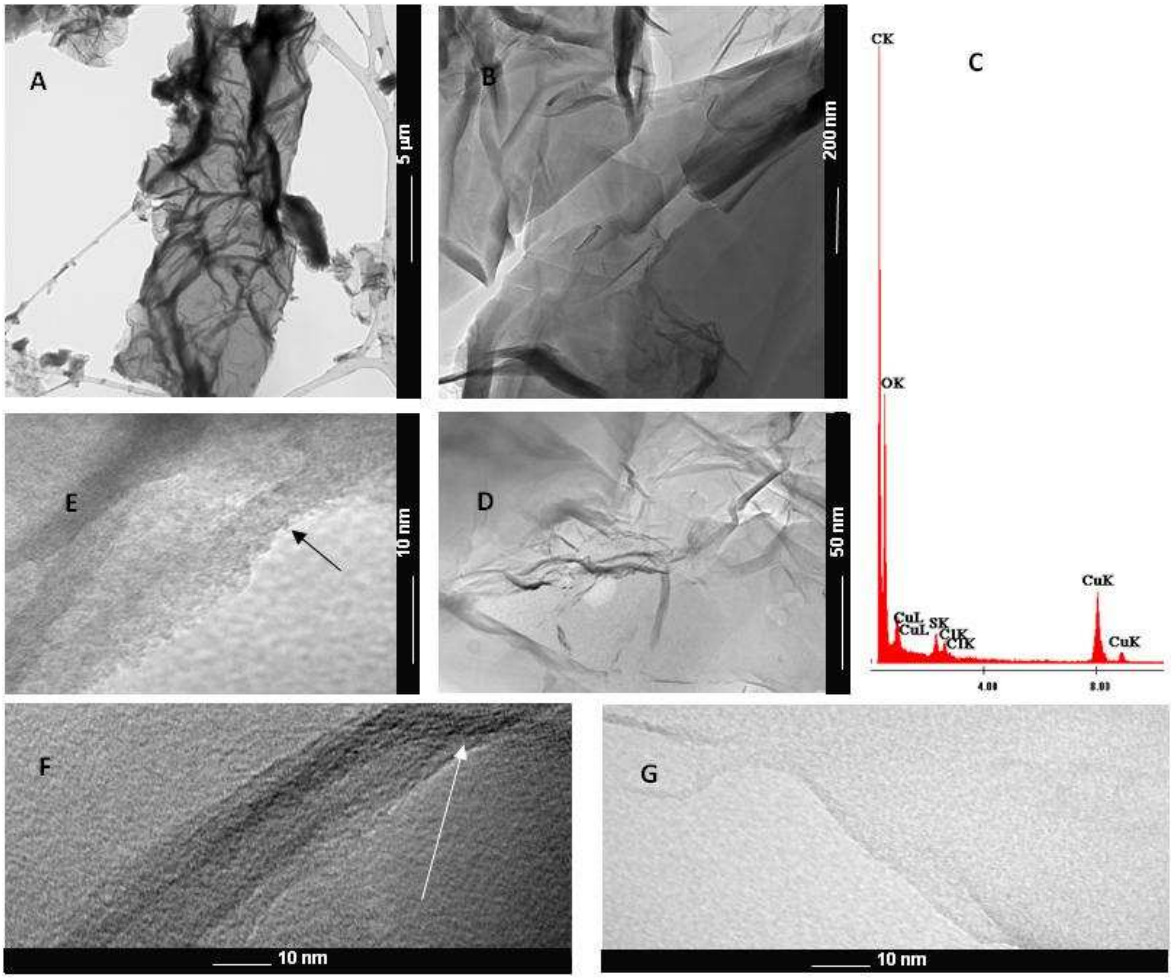

Figure 1. (A,B,D,E,F,G) TEM images of GO at different magnifications, (C) EDX spectrum taken in the area indicated with D.

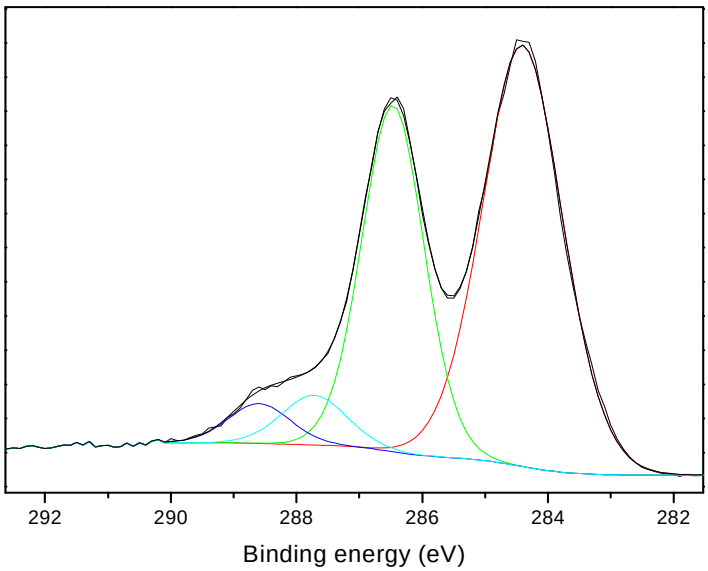

Figure 2. XPS - C 1s core level for GO.

3.2 CA-GO nanocomposites

In this part of the work, we focused our attention on the feasibility of the SC-CO_2 assisted phase inversion process on the system CA/GO/NMP. SC-CO_2 acted as a non-solvent for the polymer and the phase inversion (or separation) of the polymeric solution into two phases was obtained: one with a high polymer concentration and one with a low polymer concentration. The concentrated phase solidified shortly after phase inversion forming the porous structure. The operative parameters were selected considering a previous work on CA membranes formation by SC-CO_2 assisted phase inversion[25]; in particular, a pressure of 200 bar and a temperature of 40 °C were selected, since they represent the optimized process combination.

From a macroscopic point of view, the structures produced using CA alone, show a white color (see Figure 3A); whereas, CA structures loaded with 3 and 9% w/w GO, show an uniform black color (Figure 4A, Figure 5A).

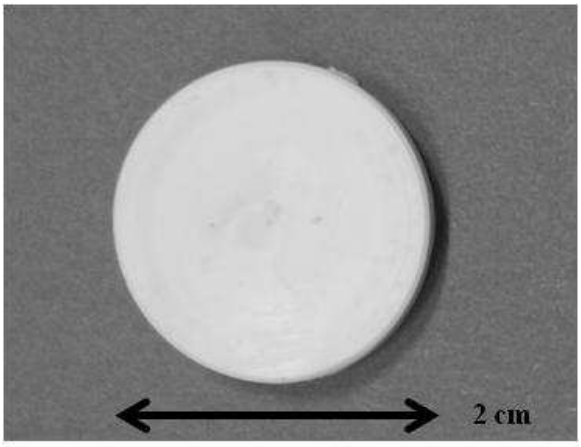

A

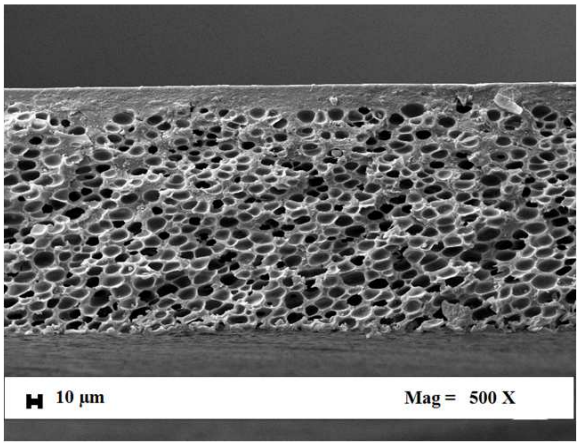

B

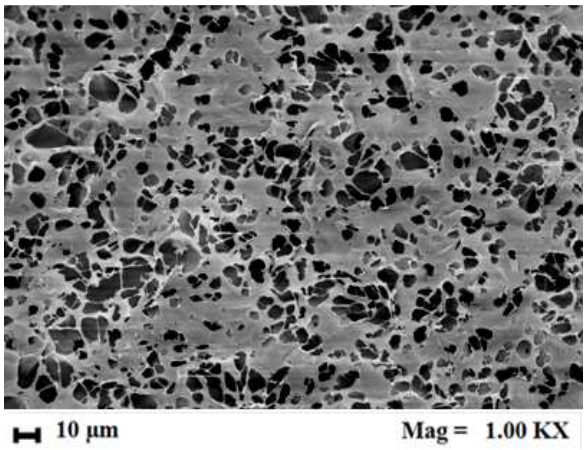

C

Figure 3. CA structures obtained at 200 bar 40 °C starting from 25% w/w CA/NMP solution: A) macroscopic view, B) FESEM analysis of the section, C) FESEM analysis of the top surface.

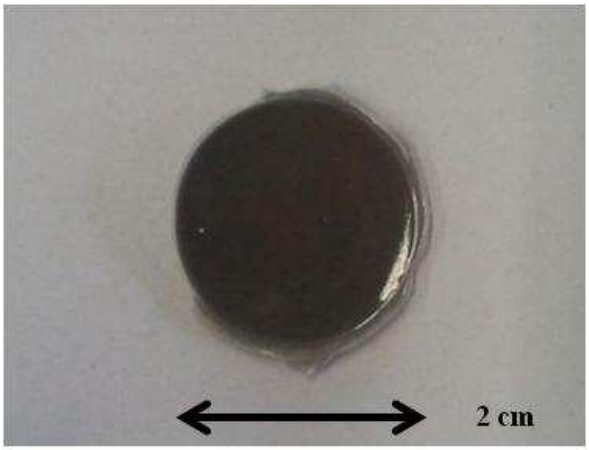

A

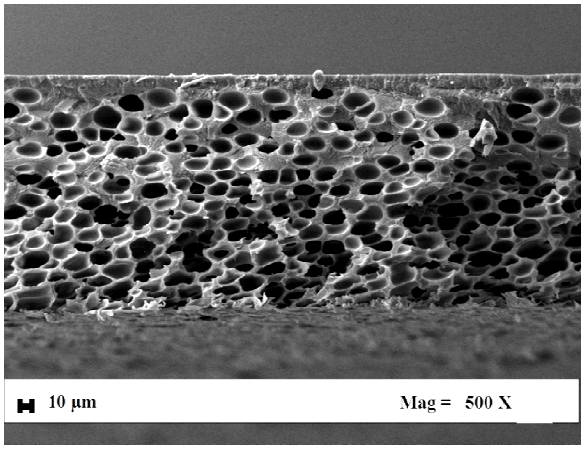

B

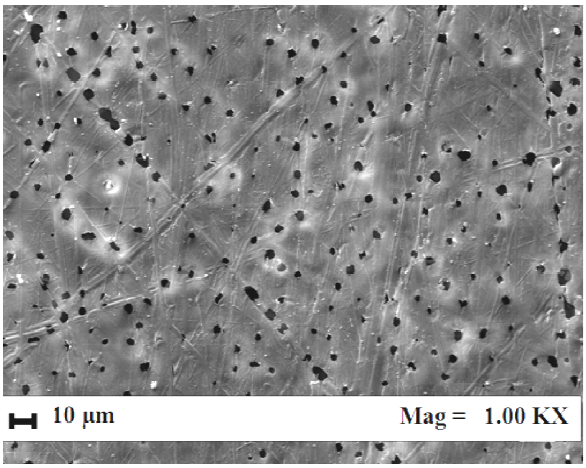

C

Figure 4. CA/GO structures obtained at 200 bar 40 °C starting from 25% w/w CA/NMP solution and 3% w/w of GO: A) macroscopic view, B) FESEM analysis of the section, C) FESEM analysis of the top surface.

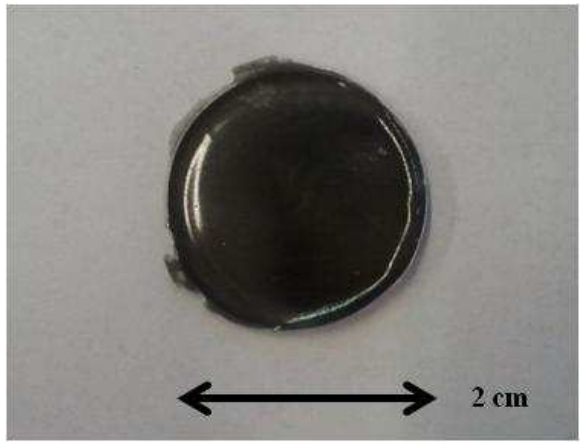

A

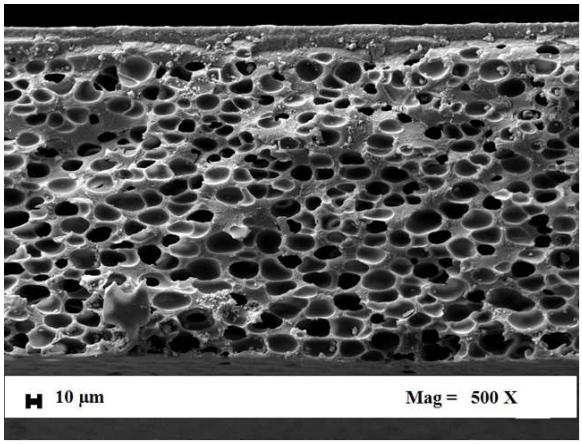

B

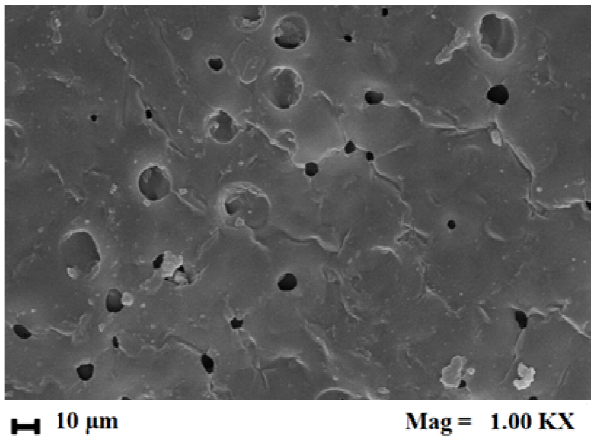

C

Figure 5. CA/GO structures obtained at 200 bar 40 °C starting from 25% w/w CA/NMP solution and 9% w/w of GO: A) macroscopic view, B) FESEM analysis of the section, C) FESEM analysis of the top surface.

From a microscopic point of view, we observed from FESEM images, that, even at the highest GO content, the section of the structures maintain the cellular morphology, characteristics of CA alone (Figure 3B compared with Figures 4B-5B). Porous top surfaces were obtained in all cases (Figures 3C-4C-5C) and a quasi-constant overall porosity (between 80-82%) was also measured. No stratification of GO towards top or bottom surfaces was observed, also at microscopic level.

DSC analyses were also performed on CA membranes and CA/GO nanocomposite structures. They showed similar traces for all treated materials, confirming that GO addition did not sensibly influence the physico-chemical characteristics of the final structures.

Summarizing, these results show that the morphology of CA structures loaded with GO is similar to those produced with pure CA; *i.e.*, GO presence does not affect the structure formation mechanism during the process assisted by SC-CO_2. Moreover, when we performed FESEM analyses at higher enlargements (up to 150000 KX), aggregates of GO were no more visible in the polymeric structure; this is an information about the dispersion of GO in the polymeric matrix even at micro/nano level. The obtained morphology (*i.e.*, cellular) suggests that nucleation and growth of droplets of the polymer-lean phase, with further solidification of the polymer-rich phase is the mechanism of the membrane formation.

Increasing the amount of GO in the starting solution, the mean pore size of the structures enlarges. This result is well evidenced by the pore size distribution reported in Figure 6 and by data in Table 1: increasing the amount of GO up to 9% w/w, the mean pore size increases from 9.2 to 16.6 μm.

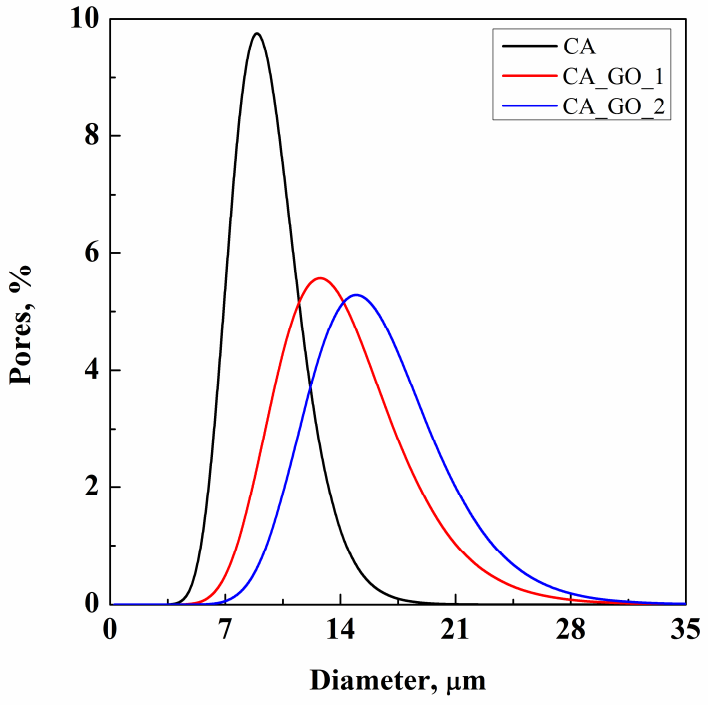

Figure 6. Pore size distribution in CA/GO nanocomposite structures obtained at different GO loadings.

Sample	**Mean pore size ± standard deviation (μm)**
CA	9.2 ± 2.1
CA_GO_1	14.0 ± 3.9
CA_GO_2	16.6 ± 4.2

Table 1. Mean pore size of CA+GO structures obtained at different GO loadings.

It indicates that even if the structures morphology has not been affected, the addition of GO plays an important role during the structure formation process. A plausible explanation for this result is that the affinity of GO with many hydrophilic groups can decrease the mass transfer between the solvent (*i.e.*, NMP) and SC-CO_2 (*i.e.*, the non-solvent) during the phase-inversion: larger pore are formed due to the slower mass transfer. This hypothesis is also

supported by the slight effect of GO content on the porosity of top surfaces. Increasing the amount of GO, the top surface porosity decreases (Figures 3C-4C-5C) and it is known that porosity of membranes surface depends on the phase separation rate: when the process is slower, the top surface tends to become “denser”; whereas, in the case of faster process, the top surface is usually “opened”.

Therefore, the addition of GO does not visibly affect thermodynamics of the phase separation process (*i.e.*, the structure formation mechanism); but, it influences the microstructure formation, acting on the kinetics of the process (*i.e.*, the phase separation rate).

Figure 7 shows two TEM images, at increasing magnification, of the polymer-GO nanocomposite. Dispersed GO nanosheets are visible in Figure 7A as black spots. Their lateral size is consistent with the starting GO sheets, as further evidenced by the high resolution TEM image (see Figure 7B).

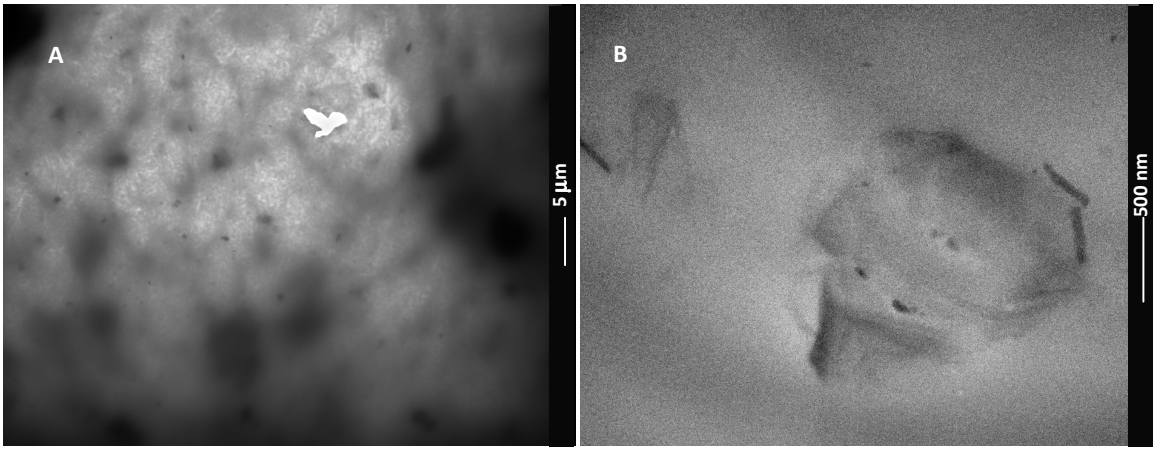

Figure 7. TEM image of CA_GO_2_8h at different magnifications.

In Figure 8 the TG-MS profiles, under a 1% v/v of O_2 in N_2 flow, of tests CA, CA_GO_1, CA_GO_2, CA_GO_2_8h, are reported as a function of temperature (the TG-MS profiles under

an air flow are shown in Figure 4S). During the thermal oxidation of CA, after an initial weak release of water ~5.0% w/w, the weight loss took place in the range 270-435 °C in which the main mass fragments of CA (m/z=15, 30, 43, 55, 61) were detected, together with m/z=18 of H_2O and m/z=44 due to the formation of CO_2. The remaining carbon is oxidized completely up to 900 °C.

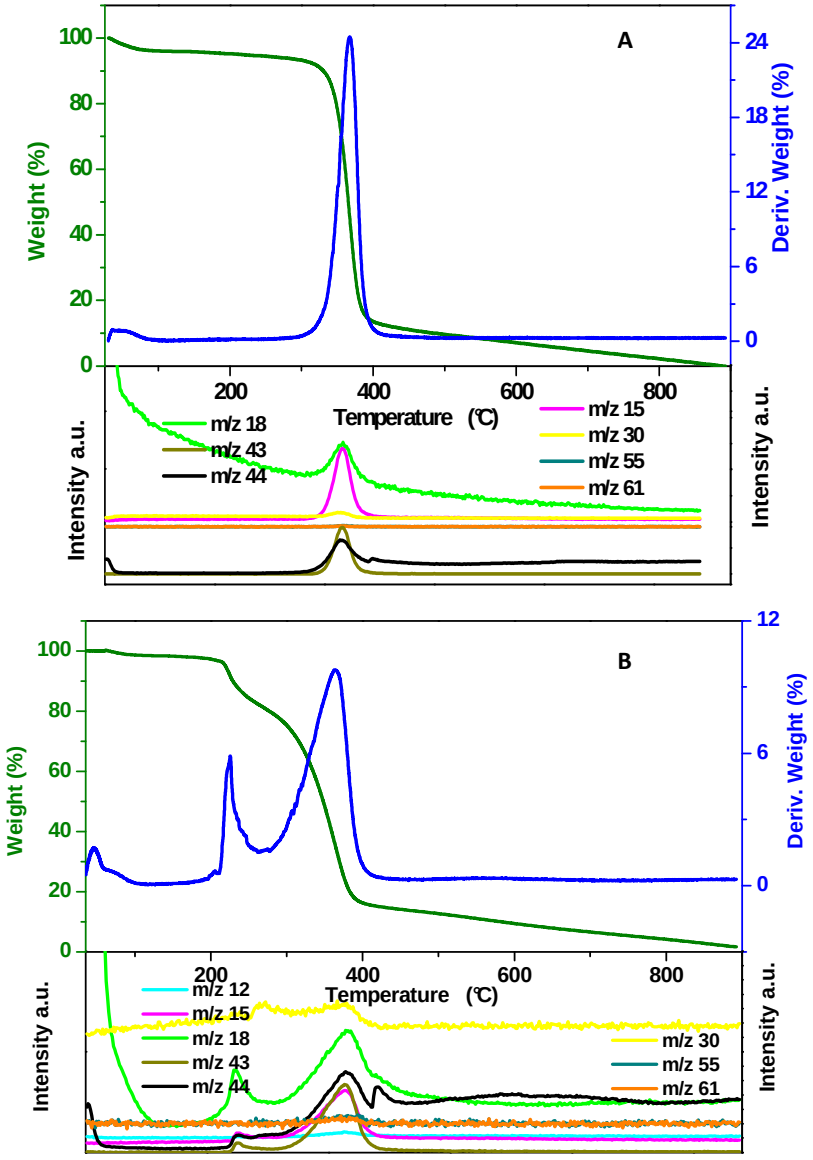

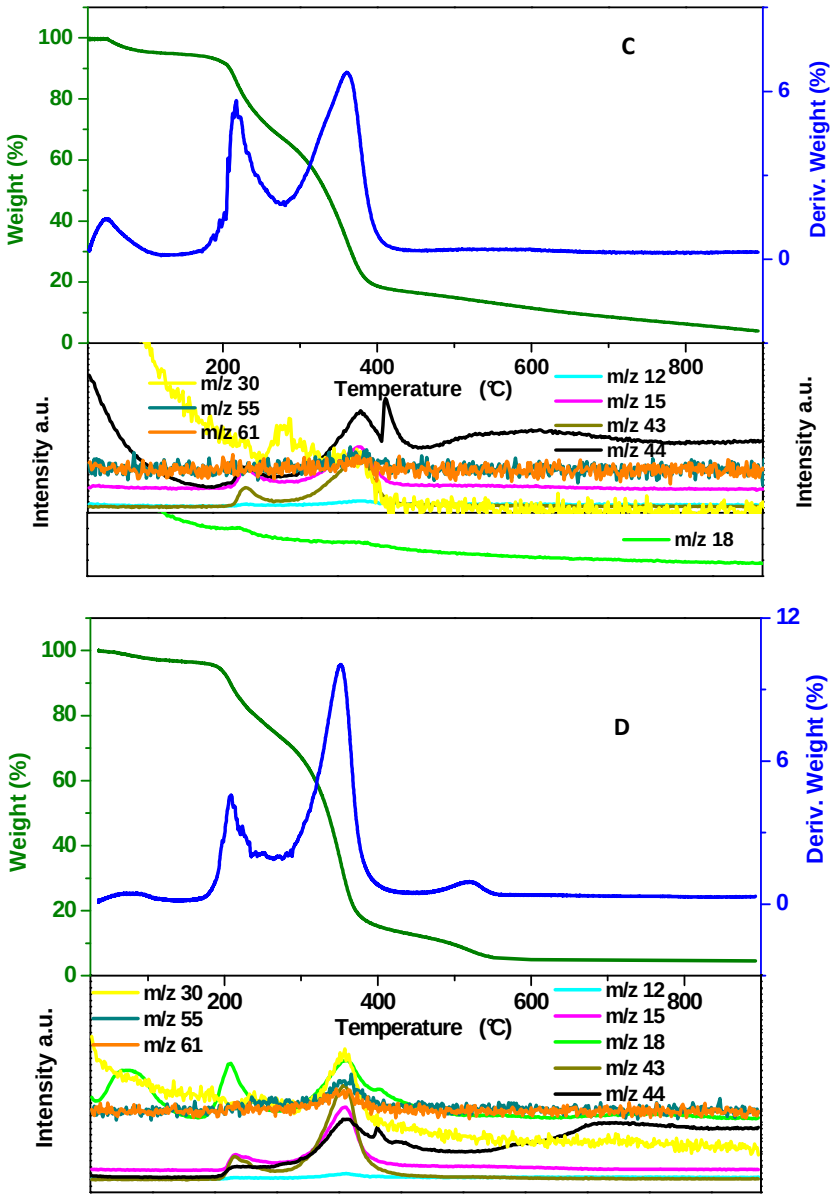

Figure 8. TG-DTG-MS profiles for CA (A), CA_GO_1 (B), CA_GO_2 (C), CA_GO_2_8h (D).

In all the nanocomposites an additional weight loss was clearly visible at lower temperature, between about 190 °C and 270 °C. It is certainly due to oxidation and decomposition, at lower temperatures in the presence of GO, of a CA fraction, as confirmed by

the evolution of its main mass fragments. It increases when GO content in the composites increases too, and decreases when SC-CO_2 processing time increases. No evidence of specific weight losses due to GO oxyfunctional groups can be seen. For all the nanocomposites, unlike CA, the residue at 900 °C is not zero; it is due to GO (see Figure 1S) and, obviously, increases with GO content, but, also with SC-CO_2 treatment times. This last observation, together with the no relevant presence of oxyfunctional groups release, suggests that the SC-CO_2 process promotes a GO partial reduction, which is probably the reason for the increased carbon skeleton amount[49] and reduced weight loss between 190 °C and 270 °C (that is probably due to CA fraction adjacent to the highly reactive functional groups of GO). This effect of SC-CO_2, though under different conditions, has been already reported[33]; but, it is the first time that it is evidenced during the incorporation in a polymeric matrix. The results also suggest that the reduction level could be modulated by varying the processing time.

No trace of SO_2 (m/z=48, 64) and Chlorine (m/z=35), initially retained in GO (see starting GO characterization), can be seen. This result evidences a further effect of SC-CO_2 processing: the ability to remove residual solvent/impurities. Therefore, all residual traces from GO preparation are removed. This capability of SC-CO_2 has been evidenced in other supercritical assisted processes, mainly SC-CO_2 drying of alginate hydrogel beads[50] and solvent elimination/killing in pharmaceutics compounds post-processing. But, it is the first time that this experimental evidence is shown for GO processing. It has very interesting implications from the point of view of GO purification and compatibilization with a biological environment, since Sulphur and Chlorine residues are cytotoxic.

To better understand the evolution of GO under SC-CO_2 process conditions, CA from CA_GO_2_8h was dissolved in NMP and the TG-MS profiles, under a 1% v/v of O_2 in N_2 flow, of the recovered GO, has been reported as a function of temperature in Figure 9. The

weight loss due to the oxyfunctional groups results clearly reduced (compare with Figure 1S)[51]; moreover, the residue is considerably increased, likely due to a GO reduction. For GO thermal reduction under vacuum it has been reported[52] that upon progressive thermal treatment: first of all, the in-plane -COOH groups become highly unstable, followed by a formation of phenolic groups and rapid removal of edge plane -C=0 at T<400 °C and basal plane -C=0 groups at T>400 °C, finally resulting in a little survival of phenolic groups. The profile of H_2O (m/z=18) (Figure 9 bottom) observed in the temperature range 120-200 °C, for the recovered GO, likely suggests that it has reached an advanced level of reduction in which the surviving species are prevalently carbonyl groups. No trace of SO_2 (m/z=48, 64) and Chlorine (m/z=35), initially retained in GO, can be seen, as already shown by the nanocomposites thermal analysis. Starting from the thermogravimetric residue in Figure 8D (4.85% w/w, that is due to GO) and that in Figure 9, we also measured the approximate GO amount in CA_GO_2_8h, that is 6.26% w/w.

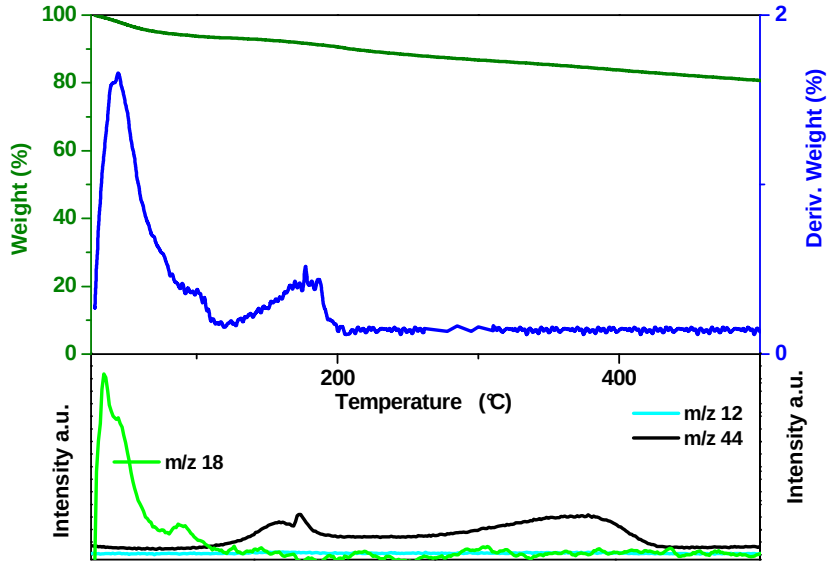

Figure 9. TG-DTG-MS profiles for GO, from CA_GO_2_8h, after CA removal in NMP.

Figure 5S and Figure 10A show XRD patterns of the GO powder films obtained after CA structure dissolution in NMP, from CA_GO_2 and CA_GO_2_8h, respectively. The peak at 8.9° (compared to Figure 3SA) is broader and shows an upshifted endset, a broad peak in the range 20-30 2θ became more and more visible[53, 54] with increasing SC-CO_2 process time indicating a partial reduction of GO[51, 53-56] due to removal of oxyfunctional groups and intercalated water, and confirming the indication of TG-MS analysis. It should be noted that it is similar to that of graphite. The peak, however, was rather broad with respect to that observed in the graphite XRD pattern.

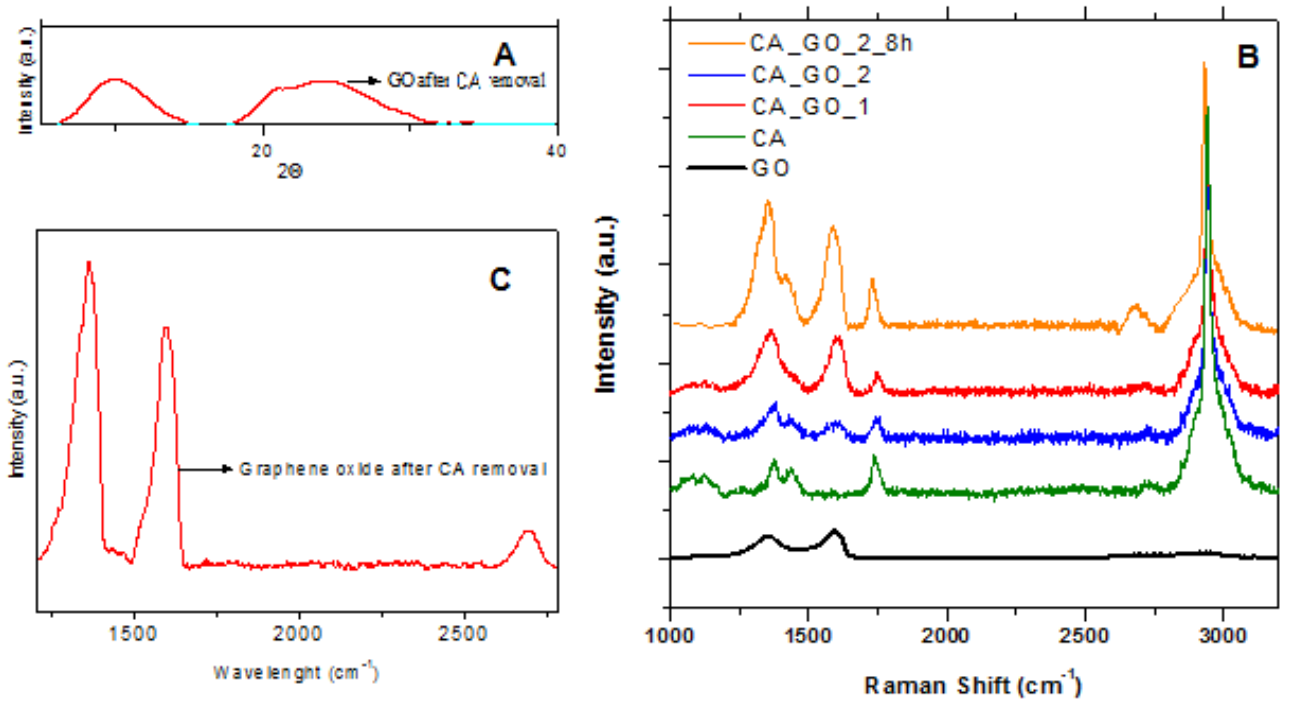

Figure 10. X-ray diffraction pattern of GO, from CA_GO_2_8h, after a CA removal in NMP (A); Raman Spectra of CA, CA_GO_1, CA_GO_2, CA_GO_2_8h (B) and GO, from CA_GO_2_8h, after a CA dissolution in NMP (C).

Raman spectra of CA and of the nanocomposites, in the wavenumber range 1000-3200 cm^{-1}, are shown in Figure 10B. Spectrum in green exhibits typical Raman modes of CA. Both CA_GO_1 and CA_GO_2 show an additional Raman line at 1593 cm^{-1} (the G-line, due to the in plane vibration of the C–C bonds of GO), more pronounced at higher GO loading. The other typical GO band, at 1357 cm^{-1} (D line), is partially superimposed to the band at 1370 cm^{-1} of CA. In CA_GO_2_8h the G band down-shifts to a position close to the G band of graphite (1586 cm^{-1}), this is typical of reduced graphene[54] and can be attributed to graphitic "self-healing"[57], while the 2D band is more pronounced[58]. The Raman spectrum of GO, after the dissolution of CA in NMP, is shown in Figure 10C; as observed in CA_GO_2_8h, the G line is down-shifted and 2D band more pronounced. Moreover, D band at 1357 cm^{-1} becomes prominent, indicating that SC-CO_2 process influences the size of the in-plane sp^2 domains[59]. In particular, an I_D/I_G ratio of 1.25 can be measured, indicating an increasing L_D distance[59, 60]. This value suggests again a partial GO reduction, in agreement with the results of TG-MS and XRD measurements, for reduced graphene oxide (rGO). Cui *et al.*[52] found an I_D/I_G ratio of 1.4, a value of 1.9 was observed for rGO reduced by HI at 100 °C[61]. However, it is difficult to compare the results, since the measurements are often recorded on GO with different edge thickness[60, 62].

4. CONCLUSIONS AND PERSPECTIVES

Homogeneous CA/GO nanocomposites were successfully prepared using a SC-CO_2 assisted phase inversion, confirming the ability of supercritical processing to treat polymeric suspensions preventing stratification phenomena. The structures exhibited the cellular morphology observed for CA membranes, also at the highest GO loadings (9% w/w).

Moreover, a partial reduction of GO to graphene was also observed for the first time and S and Cl impurities, that were present in the starting GO material, were completely eliminated by SC-CO_2 during the structures formation, producing an improved material. This result is new and it can be very useful, for example, for biomedical applications of GO.

ACKNOWLEDGEMENTS

The authors thank Eng. Claudia Cirillo for the Raman Spectroscopy measurements.

SUPPORTING INFORMATION

In Supporting Information, we reported the TG-MS profiles of GO under air flow and under a 1% v/v of O_2 in N_2 flow, the XRD of starting Graphite and of GO and Raman Spectrum of GO, the TG-MS profiles of CA-GO nanocomposites under air flow and the X-ray diffraction pattern of GO after CA removal, to complete the characterization.

This information is available free of charge via the Internet at http://pubs.acs.org/.

REFERENCES

(1) Hummers Jr, W. S.; Offeman, R. E. Preparation of graphitic oxide. *J. Am. Chem. Soc.* **1958,** *80*, 1339.

(2) Du, J.; Cheng, H. M. The fabrication, properties, and uses of graphene/polymer composites. *Macromol. Chem. Phys.* **2012,** *213*, 1060.

(3) Marcano, D. C.; Kosynkin, D. V.; Berlin, J. M.; Sinitskii, A.; Sun, Z.; Slesarev, A.; Alemany, L. B.; Lu, W.; Tour, J. M. Improved synthesis of graphene oxide. *ACS nano* **2010,** *4*, 4806.

(4) An, X.; Simmons, T.; Shah, R.; Wolfe, C.; Lewis, K. M.; Washington, M.; Nayak, S. K.; Talapatra, S.; Kar, S. Stable aqueous dispersions of noncovalently functionalized graphene from graphite and their multifunctional high-performance applications. *Nano Lett.* **2010,** *10*, 4295.

(5) Cao, Y.-C.; Xu, C.; Wu, X.; Wang, X.; Xing, L.; Scott, K. A poly (ethylene oxide)/graphene oxide electrolyte membrane for low temperature polymer fuel cells. *J. Power Sources* **2011,** *196*, 8377.

(6) Ganesh, B.; Isloor, A. M.; Ismail, A. Enhanced hydrophilicity and salt rejection study of graphene oxide-polysulfone mixed matrix membrane. *Desalination* **2013,** *313*, 199.

(7) Wang, Z.; Yu, H.; Xia, J.; Zhang, F.; Li, F.; Xia, Y.; Li, Y. Novel GO-blended PVDF ultrafiltration membranes. *Desalination* **2012,** *299*, 50.

(8) Maroudas, N. Sulphonated polystyrene as an optimal substratum for the adhesion and spreading of mesenchymal cells in monovalent and divalent saline solutions. *J. Cell. Physiol.* **1977,** *90*, 511.

(9) Tidwell, C. D.; Ertel, S. I.; Ratner, B. D.; Tarasevich, B. J.; Atre, S.; Allara, D. L. Endothelial cell growth and protein adsorption on terminally functionalized, self-assembled monolayers of alkanethiolates on gold. *Langmuir* **1997,** *13*, 3404.

(10) Depan, D.; Misra, R. The interplay between nanostructured carbon-grafted chitosan scaffolds and protein adsorption on the cellular response of osteoblasts: Structure–function property relationship. *Acta Biomater.* **2013,** *9*, 6084.

(11) Yoon, O. J.; Jung, C. Y.; Sohn, I. Y.; Kim, H. J.; Hong, B.; Jhon, M. S.; Lee, N.-E. Nanocomposite nanofibers of poly (d, l-lactic-co-glycolic acid) and graphene oxide nanosheets. *Composites, Part A* **2011,** *42*, 1978.

(12) Ma, H.; Su, W.; Tai, Z.; Sun, D.; Yan, X.; Liu, B.; Xue, Q. Preparation and cytocompatibility of polylactic acid/hydroxyapatite/graphene oxide nanocomposite fibrous membrane. *Chin. Sci. Bull.* **2012,** *57*, 3051.

(13) Ionita, M.; Pandele, M. A.; Iovu, H. Sodium alginate/graphene oxide composite films with enhanced thermal and mechanical properties. *Carbohydr. Polym.* **2013,** *94*, 339.

(14) Ionita, M.; Pandele, A. M.; Crica, L.; Pilan, L. Improving the thermal and mechanical properties of polysulfone by incorporation of graphene oxide. *Composites, Part B* **2014,** *59*, 133.

(15) Pandele, A. M.; Ionita, M.; Crica, L.; Dinescu, S.; Costache, M.; Iovu, H. Synthesis, characterization, and in vitro studies of graphene oxide/chitosan–polyvinyl alcohol films. *Carbohydr. Polym.* **2014,** *102*, 813.

(16) Paredes, J.; Villar-Rodil, S.; Martinez-Alonso, A.; Tascon, J. Graphene oxide dispersions in organic solvents. *Langmuir* **2008,** *24*, 10560.

(17) Sarno, M.; Senatore, A.; Cirillo, C.; Petrone, V.; Ciambelli, P. Oil lubricant tribological behaviour improvement through dispersion of few layer graphene oxide. *J. Nanosci. Nanotechnol.* **2014,** *14*, 4960.

(18) Schniepp, H. C.; Li, J.-L.; McAllister, M. J.; Sai, H.; Herrera-Alonso, M.; Adamson, D. H.; Prud'homme, R. K.; Car, R.; Saville, D. A.; Aksay, I. A. Functionalized single graphene sheets derived from splitting graphite oxide. *J. Phys. Chem. B* **2006,** *110*, 8535.

(19) Zhu, Y.; Stoller, M. D.; Cai, W.; Velamakanni, A.; Piner, R. D.; Chen, D.; Ruoff, R. S. Exfoliation of graphite oxide in propylene carbonate and thermal reduction of the resulting graphene oxide platelets. *ACS nano* **2010,** *4*, 1227.

(20) De Marco, I.; Knauer, O.; Cice, F.; Braeuer, A.; Reverchon, E. Interactions of phase equilibria, jet fluid dynamics and mass transfer during supercritical antisolvent micronization: The influence of solvents. *Chem. Eng. J.* **2012,** *203*, 71.

(21) Reverchon, E.; Adami, R. Supercritical assisted atomization to produce nanostructured chitosan-hydroxyapatite microparticles for biomedical application. *Powder Technol.* **2013,** *246*, 441.

(22) Campardelli, R.; Baldino, L.; Reverchon, E. Supercritical fluids applications in nanomedicine. *J. Supercrit. Fluids* **2015,** *101*, 193.

(23) Reverchon, E.; De Marco, I. Supercritical fluid extraction and fractionation of natural matter. *J. Supercrit. Fluids* **2006,** *38*, 146.

(24) Baldino, L.; Cardea, S.; De Marco, I.; Reverchon, E. Chitosan scaffolds formation by a supercritical freeze extraction process. *J. Supercrit. Fluids* **2014,** *90*, 27.

(25) Reverchon, E.; Cardea, S. Formation of cellulose acetate membranes using a supercritical fluid assisted process. *J. Membr. Sci.* **2004,** *240*, 187.

(26) Reverchon, E.; Rappo, E. S.; Cardea, S. Flexible supercritical CO2-assisted process for poly (methyl methacrylate) structure formation. *Polym. Eng. Sci.* **2006,** *46*, 188.

(27) Cardea, S.; Sessa, M.; Reverchon, E. Supercritical CO 2 assisted formation of poly (vinylidenefluoride) aerogels containing amoxicillin, used as controlled release device. *J. Supercrit. Fluids* **2011,** *59*, 149.

(28) Cardea, S.; Reverchon, E. Nanostructured PVDF-HFP membranes loaded with catalyst obtained by supercritical CO 2 assisted techniques. *Chem. Eng. Process.* **2011,** *50*, 630.

(29) Baldino, L.; Cardea, S.; Reverchon, E. Supercritical assisted enzymatic membranes preparation, for active packaging applications. *J. Membr. Sci.* **2014,** *453*, 409.

(30) Lee, C.; Wei, X.; Kysar, J. W.; Hone, J. Measurement of the elastic properties and intrinsic strength of monolayer graphene. *Science* **2008,** *321*, 385.

(31) Li, L.; Zheng, X.; Wang, J.; Sun, Q.; Xu, Q. Solvent-exfoliated and functionalized graphene with assistance of supercritical carbon dioxide. *ACS Sustainable Chem. Eng.* **2012,** *1*, 144.

(32) Pu, N.-W.; Wang, C.-A.; Sung, Y.; Liu, Y.-M.; Ger, M.-D. Production of few-layer graphene by supercritical CO 2 exfoliation of graphite. *Mater. Lett.* **2009,** *63*, 1987.

(33) Rangappa, D.; Sone, K.; Wang, M.; Gautam, U. K.; Golberg, D.; Itoh, H.; Ichihara, M.; Honma, I. Rapid and Direct Conversion of Graphite Crystals into High-Yielding, Good-Quality Graphene by Supercritical Fluid Exfoliation. *Chem. Eur. J.* **2010,** *16*, 6488.

(34) Omi, H.; Ueda, T.; Miyakubo, K.; Eguchi, T. Dynamics of CO 2 Molecules Confined in the Micropores of Solids as Studied by 13 C NMR. *Appl. Surf. Sci.* **2005,** *252*, 660.

(35) Mayer-Wagner, S.; Schiergens, T.; Sievers, B.; Redeker, J.; Schmitt, B.; Buettner, A.; Jansson, V.; Müller, P. Scaffold-free 3D cellulose acetate membrane-based cultures form large cartilaginous constructs. *J. Tissue Eng. Regener. Med.* **2011,** *5*, 151.

(36) Du, J.; Tan, E.; Kim, H. J.; Zhang, A.; Bhattacharya, R.; Yarema, K. J. Comparative evaluation of chitosan, cellulose acetate, and polyethersulfone nanofiber scaffolds for neural differentiation. *Carbohydr. Polym.* **2014,** *99*, 483.

(37) Entcheva, E.; Bien, H.; Yin, L.; Chung, C.-Y.; Farrell, M.; Kostov, Y. Functional cardiac cell constructs on cellulose-based scaffolding. *Biomaterials* **2004,** *25*, 5753.

(38) Idris, A.; Yet, L. K. The effect of different molecular weight PEG additives on cellulose acetate asymmetric dialysis membrane performance. *J. Membr. Sci.* **2006,** *280*, 920.

(39) Kutowy, O.; Sourirajan, S. Cellulose acetate ultrafiltration membranes. *J. Appl. Polym. Sci.* **1975,** *19*, 1449.

(40) Bose, S.; Kuila, T.; Uddin, M. E.; Kim, N. H.; Lau, A. K.; Lee, J. H. In-situ synthesis and characterization of electrically conductive polypyrrole/graphene nanocomposites. *Polymer* **2010,** *51*, 5921.

(41) Chai, B.; Li, J.; Xu, Q.; Dai, K. Facile synthesis of reduced graphene oxide/WO 3 nanoplates composites with enhanced photocatalytic activity. *Mater. Lett.* **2014,** *120*, 177.

(42) Yu, W.; Fu, J.; Dong, X.; Chen, L.; Shi, L. A graphene hybrid material functionalized with POSS: Synthesis and applications in low-dielectric epoxy composites. *Compos. Sci. Technol.* **2014,** *92*, 112.

(43) Gonçalves, G.; Vila, M.; Bdikin, I.; de Andrés, A.; Emami, N.; Ferreira, R. A.; Carlos, L. D.; Grácio, J.; Marques, P. A. Breakdown into nanoscale of graphene oxide: Confined hot spot atomic reduction and fragmentation. *Sci. Rep.* **2014,** *4*.

(44) Shen, X.; Lin, X.; Yousefi, N.; Jia, J.; Kim, J.-K. Wrinkling in graphene sheets and graphene oxide papers. *Carbon* **2014,** *66*, 84.

(45) Ma, X.; Zachariah, M. R.; Zangmeister, C. D. Crumpled nanopaper from graphene oxide. *Nano Lett.* **2011,** *12*, 486.

(46) Kim, F.; Cote, L. J.; Huang, J. Graphene Oxide: Surface Activity and Two-Dimensional Assembly. *Adv. Mater.* **2010,** *22*, 1954.

(47) Eigler, S.; Dotzer, C.; Hirsch, A. Visualization of defect densities in reduced graphene oxide. *Carbon* **2012,** *50*, 3666.

(48) Krishnamoorthy, K.; Kim, G.-S.; Kim, S. J. Graphene nanosheets: Ultrasound assisted synthesis and characterization. *Ultrason. Sonochem.* **2013,** *20*, 644.

(49) Ganguly, A.; Sharma, S.; Papakonstantinou, P.; Hamilton, J. Probing the thermal deoxygenation of graphene oxide using high-resolution in situ X-ray-based spectroscopies. *J. Phys. Chem. C* **2011,** *115*, 17009.

(50) Della Porta, G.; Del Gaudio, P.; De Cicco, F.; Aquino, R. P.; Reverchon, E. Supercritical drying of alginate beads for the development of aerogel biomaterials: optimization of process parameters and exchange solvents. *Ind. Eng. Chem. Res.* **2013,** *52*, 12003.

(51) Park, S.; An, J.; Potts, J. R.; Velamakanni, A.; Murali, S.; Ruoff, R. S. Hydrazine-reduction of graphite-and graphene oxide. *Carbon* **2011,** *49*, 3019.

(52) Cui, P.; Lee, J.; Hwang, E.; Lee, H. One-pot reduction of graphene oxide at subzero temperatures. *Chem. Commun.* **2011,** *47*, 12370.

(53) Serhatkulu, G. K.; Dilek, C.; Gulari, E. Supercritical CO 2 intercalation of layered silicates. *J. Supercrit. Fluids* **2006,** *39*, 264.

(54) Wojtoniszak, M.; Chen, X.; Kalenczuk, R. J.; Wajda, A.; Łapczuk, J.; Kurzewski, M.; Drozdzik, M.; Chu, P. K.; Borowiak-Palen, E. Synthesis, dispersion, and cytocompatibility of graphene oxide and reduced graphene oxide. *Colloids Surf., B* **2012,** *89*, 79.

(55) Shin, H. J.; Kim, K. K.; Benayad, A.; Yoon, S. M.; Park, H. K.; Jung, I. S.; Jin, M. H.; Jeong, H. K.; Kim, J. M.; Choi, J. Y. Efficient reduction of graphite oxide by sodium borohydride and its effect on electrical conductance. *Adv. Funct. Mater.* **2009,** *19*, 1987.

(56) Compton, O. C.; Jain, B.; Dikin, D. A.; Abouimrane, A.; Amine, K.; Nguyen, S. T. Chemically active reduced graphene oxide with tunable C/O ratios. *ACS nano* **2011,** *5*, 4380.

(57) Kudin, K. N.; Ozbas, B.; Schniepp, H. C.; Prud'Homme, R. K.; Aksay, I. A.; Car, R. Raman spectra of graphite oxide and functionalized graphene sheets. *Nano lett.* **2008,** *8*, 36.

(58) Ciambelli, P.; Sarno, M.; Gorrasi, G.; Sannino, D.; Tortora, M.; Vittoria, V. Preparation and physical properties of carbon nanotubes–PVA nanocomposites. *J. Macromol. Sci., Part B: Phys.* **2005,** *44*, 779.

(59) Barroso-Bujans, F.; Alegría, Á.; Colmenero, J. Kinetic study of the graphite oxide reduction: combined structural and gravimetric experiments under isothermal and nonisothermal conditions. *J. Phys. Chem. C* **2010,** *114*, 21645.

(60) Sarno, M.; Cirillo, C.; Piscitelli, R.; Ciambelli, P. A study of the key parameters, including the crucial role of H 2 for uniform graphene growth on Ni foil. *J. Mol. Catal. A: Chem.* **2013,** *366*, 303.

(61) Pei, S.; Zhao, J.; Du, J.; Ren, W.; Cheng, H.-M. Direct reduction of graphene oxide films into highly conductive and flexible graphene films by hydrohalic acids. *Carbon* **2010,** *48*, 4466.

(62) Erickson, K.; Erni, R.; Lee, Z.; Alem, N.; Gannett, W.; Zettl, A. Determination of the local chemical structure of graphene oxide and reduced graphene oxide. *Adv. Mater.* **2010,** *22*, 4467.

FOR TABLE OF CONTENTS ONLY